

# Supplementary Material for "SPECFEM2D-DG, an Open Source Software Modeling Mechanical Waves in Coupled Solid-Fluid Systems: the Linearised Navier-Stokes Approach"

Léo Martire<sup>1\*</sup>, R. Martin<sup>2</sup>, Q. Brissaud<sup>3</sup>, R. F. Garcia<sup>1</sup>

<sup>1</sup> ISAE-SUPAERO, Toulouse, France

<sup>2</sup> OMP-GET, Toulouse, France

<sup>3</sup> California Institute of Technology, Pasadena, CA 91125, USA

19 May 2021

## 1 CONTENTS

- Figures S1 to S6.
- Table S1.

## REFERENCES

- Arina, R., 2016. Validation of a Discontinuous Galerkin Implementation of the Time-Domain Linearized Navier–Stokes Equations for Aeroacoustics, *Aerospace*, **3**(1), 7.
- Bass, H. E. & Chambers, J. P., 2001. Absorption of sound in the Martian atmosphere, *The Journal of the Acoustical Society of America*, **109**(6), 3069–3071.
- Drob, D. P., Emmert, J. T., Meriwether, J. W., Makela, J. J., Doornbos, E., Conde, M., Hernandez, G., Noto, J., Zawdie, K. A., McDonald, S. E., Huba, J. D., & Klenzing, J. H., 2015. An update to the Horizontal Wind Model (HWM): The quiet time thermosphere, *Earth and Space Science*, **2**(7), 301–319.
- Emmert, J. T., Drob, D. P., Picone, J. M., Siskind, D. E., Jones, M., Mlynczak, M. G., Bernath, P. F., Chu, X., Doornbos, E., Funke, B., Goncharenko, L. P., Hervig, M. E., Schwartz, M. J., Sheese, P. E., Vargas, F., Williams, B. P., & Yuan, T., 2021. NRLMSIS 2.0: A Whole-Atmosphere Empirical Model of Temperature and Neutral Species Densities, *Earth and Space Science*, **8**(3).
- Garcia, R. F., Brissaud, Q., Rolland, L. M., Martin, R., Komatitsch, D., Spiga, A., Lognonné, P. H., & Banerdt, W. B., 2017. Finite-Difference Modeling of Acoustic and Gravity Wave Propagation in Mars Atmosphere: Application to Infrasonds Emitted by Meteor Impacts, *Space Science Reviews*, **211**(1-4), 547–570.

**Table S1.** Detailed scalar expressions of the LNS' strong formulation terms, as defined in Eq. (2). These play a role in the volume terms of the weak formulation detailed in Appendix B1. The notations are that of Eq. (2), as well as some additional ones provided in Section 3. Here, only the case  $d = 2$  is presented. Generalization to  $d = 3$  is straightforward, though more tedious to write down.

$q$	$\Sigma$	$\Sigma_x$	$\Sigma_z$	$G$	$F$
$\rho'$	$\delta_m$	$\delta_{m,x}$	$\delta_{m,z}$	0	$F_\rho$
$\rho_0 v'_x$	$[\rho_0 \mathbf{v}_0 \otimes \mathbf{v}' + p' \mathbf{I} - \mathbb{N}']_{1,:}$	$\rho_0 v_{0,x} v'_x + p' - \mathbb{N}'_{11}$	$\rho_0 v_{0,x} v'_z - \mathbb{N}'_{12}$	$\rho' g_x - (\delta_m \cdot \nabla) v_{0,x}$	$F v_x + v'_x F_\rho$
$\rho_0 v'_z$	$[\rho_0 \mathbf{v}_0 \otimes \mathbf{v}' + p' \mathbf{I} - \mathbb{N}']_{2,:}$	$\rho_0 v_{0,z} v'_x - \mathbb{N}'_{21}$	$\rho_0 v_{0,z} v'_z + p' - \mathbb{N}'_{22}$	$\rho' g_z - (\delta_m \cdot \nabla) v_{0,z}$	$F v_z + v'_z F_\rho$
$E'$	$(E_0 + p_0) \mathbf{v}' + (E' + p') \mathbf{v}_0 - \mathbb{N}^0 \mathbf{v}' - \mathbb{N}' \mathbf{v}_0 - \kappa \nabla T'$	$(E_0 + p_0 - \mathbb{N}^0_{11}) v'_x + (E' + p' - \mathbb{N}'_{11}) v_{0,x} - \mathbb{N}^0_{12} v'_z - \mathbb{N}'_{12} v_{0,z} - \kappa \partial_x T'$	$(E_0 + p_0 - \mathbb{N}^0_{22}) v'_z + (E' + p' - \mathbb{N}'_{22}) v_{0,z} - \mathbb{N}^0_{21} v'_x - \mathbb{N}'_{21} v_{0,x} - \kappa \partial_z T'$	$\mathbf{g} \cdot \delta_m$	$F_{E'}$

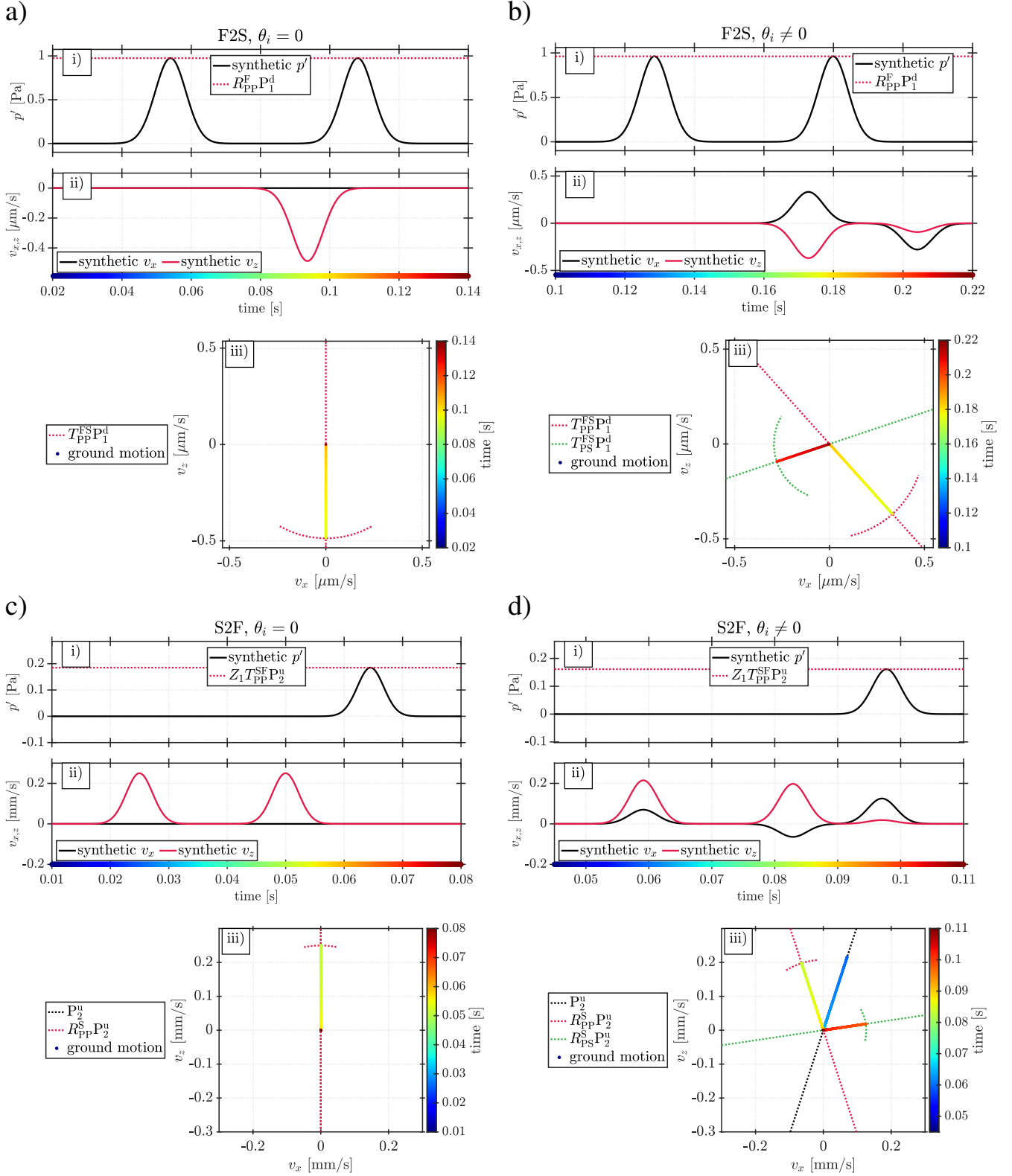


**Figure S1.** Time series comparison for the validation of the fluid-solid coupling. Panels a) and b): fluid to solid cases. Panels c) and d): solid to fluid cases. Panels a) and c): orthogonal incidence ( $i_1 = i_2 = \theta_i = 0^\circ$ ). Panels b) and d): slanted incidence ( $i_1 = i_2 = \theta_i \neq 0^\circ$ ). On all plots, time progression is colored for illustrative purposes.  $P_2^u$  denotes the velocity amplitude of the up-going elastic P-wave in the S2F case, while  $P_1^d$  denotes the velocity amplitude of the down-going acoustic P-wave in the F2S case. For each panel, the sub-panel i) displays pressure perturbation time series, the sub-panel ii) shows horizontal/vertical ground motion, and the sub-panel iii) presents the ground motion polarization. On sub-panels i), the red dotted lines represent either the expected reflected amplitude  $R_{PP}^E P_1^d$  for the F2S case (panels a) and b) or the expected transmitted amplitude  $Z_1 T_{PP}^{SE} P_2^u$  for the S2F case (panels c) and d); see Table 2. On sub-panels iii), the dotted lines highlight the expected incident (black, if applicable), and transmitted/reflected P (red) or S (green) angles; the respective expected amplitudes (see Table 2) are displayed with circle segments.

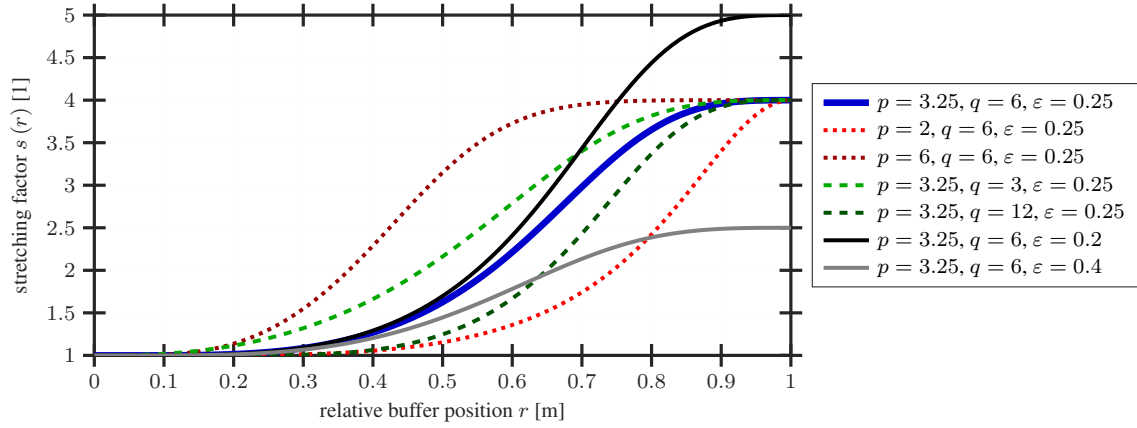


**Figure S2.** Arina (2016)'s stretching functions. The stretching function is defined in Eq. (D.12). The dependency of the function on its parameters ( $p$ ,  $q$ , and  $\varepsilon$ ) is illustrated here. The choice for the validation presented in Appendix D2 is the blue thick solid line.

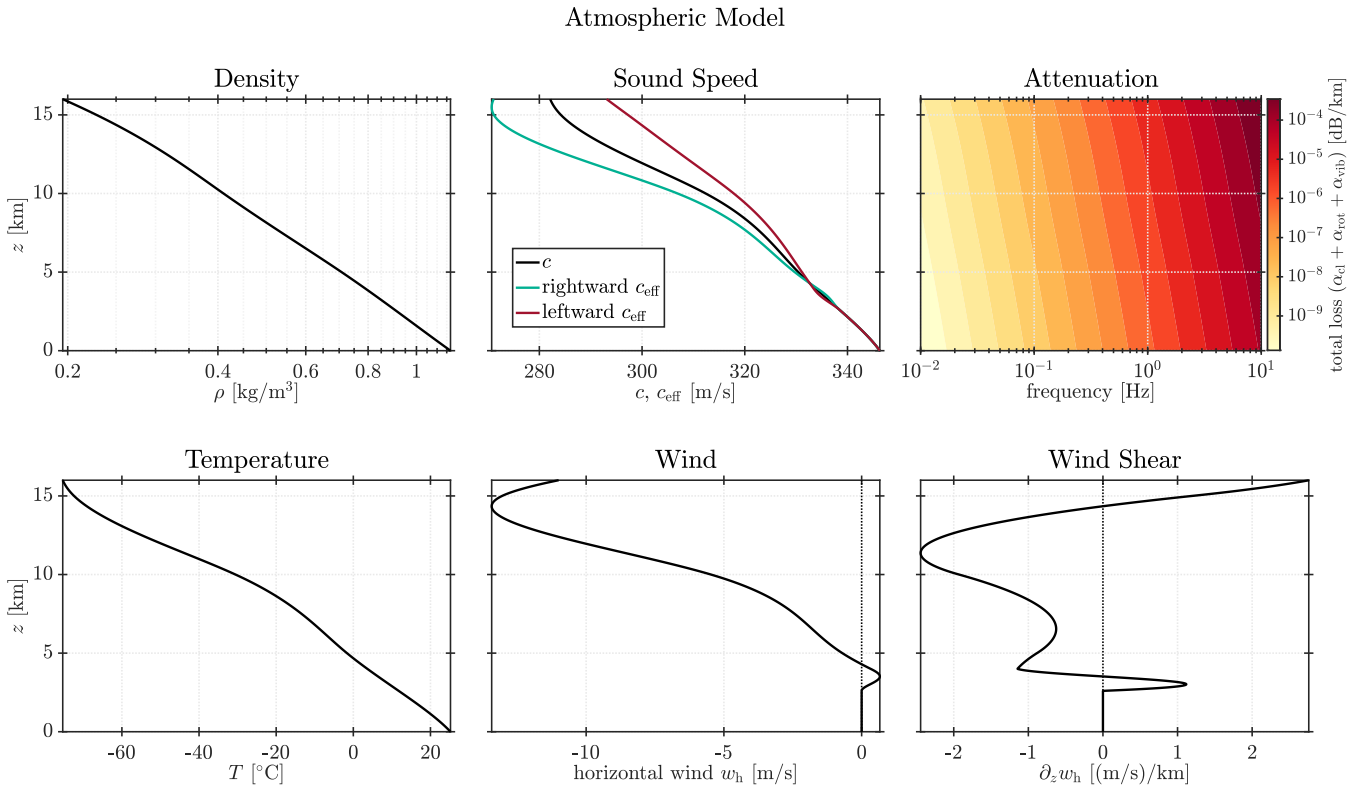


**Figure S3.** Realistic atmospheric model associated to the realistic topography case. It is computed from the MSIS20 and HWM14 models (Emmert et al. 2021; Drob et al. 2015), at the midpoint of the considered cross-section ( $42.6^\circ\text{N}$ ,  $0.3^\circ\text{E}$ ), and on 2000/07/15 at 23:00 UTC (chosen due to get the strongest winds). The "leftward" and "rightward" keywords are given in the context of this simulation: "rightward" means towards the North, and "leftward" means towards the South. The leftward propagation undergoes the strongest winds. The attenuation coefficients (in dB/km) are computed using the relations presented, e.g., in the works of (Bass & Chambers 2001) or (Garcia et al. 2017). Vibrational attenuation is negligible here  $\alpha_{\text{vib}} \simeq 0$ .

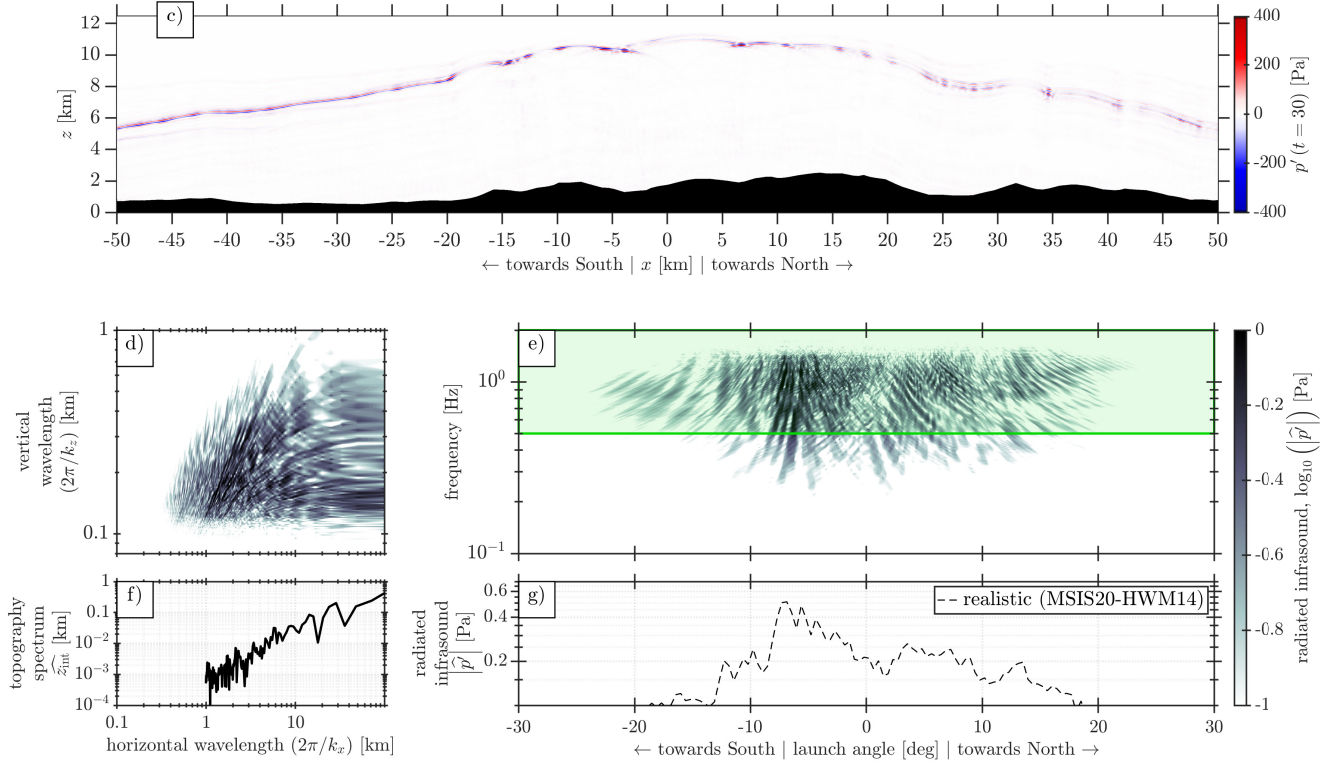


**Figure S4.** Summary of the scattering and radiation pattern study for the realistic topography case, with the atmosphere presented in Figure S3. See also Figure 7 in the main text for comparison. For the chosen cross-section, see panels a) and b) of Figure 7 in the main text. Panels c) to g) present results from the SPECIFEM2D-DG-LNS simulation under the realistic atmosphere. Panels c) to f) for the isothermal atmosphere do not differ significantly and are presented in Figure 7 in the main text. Panel c): SPECIFEM2D-DG-LNS synthetic pressure field above the chosen topography, at  $t = 30$  s. Panels d) and e): pressure perturbation spectrum computed as the 2D Fourier transform of the pressure field. Panel d): one-sided pressure spectrum in the wavelength space  $|\hat{p}'(-k_x, k_z)| + |\hat{p}'(k_x, k_z)|$ . Panel e): full two-sided pressure spectrum presented in the frequency-incidence space (see description in Section 8.2). Panel f): topography spectrum computed as the Fourier transform of the fluid-solid interface  $z_{\text{int}}$ . Panel g): amount of radiated energy, as function of launch angle, in the infrasound band (0.5–2 Hz, highlighted in green in panel e)), for the realistic atmospheric model.

## Atmospheric Model

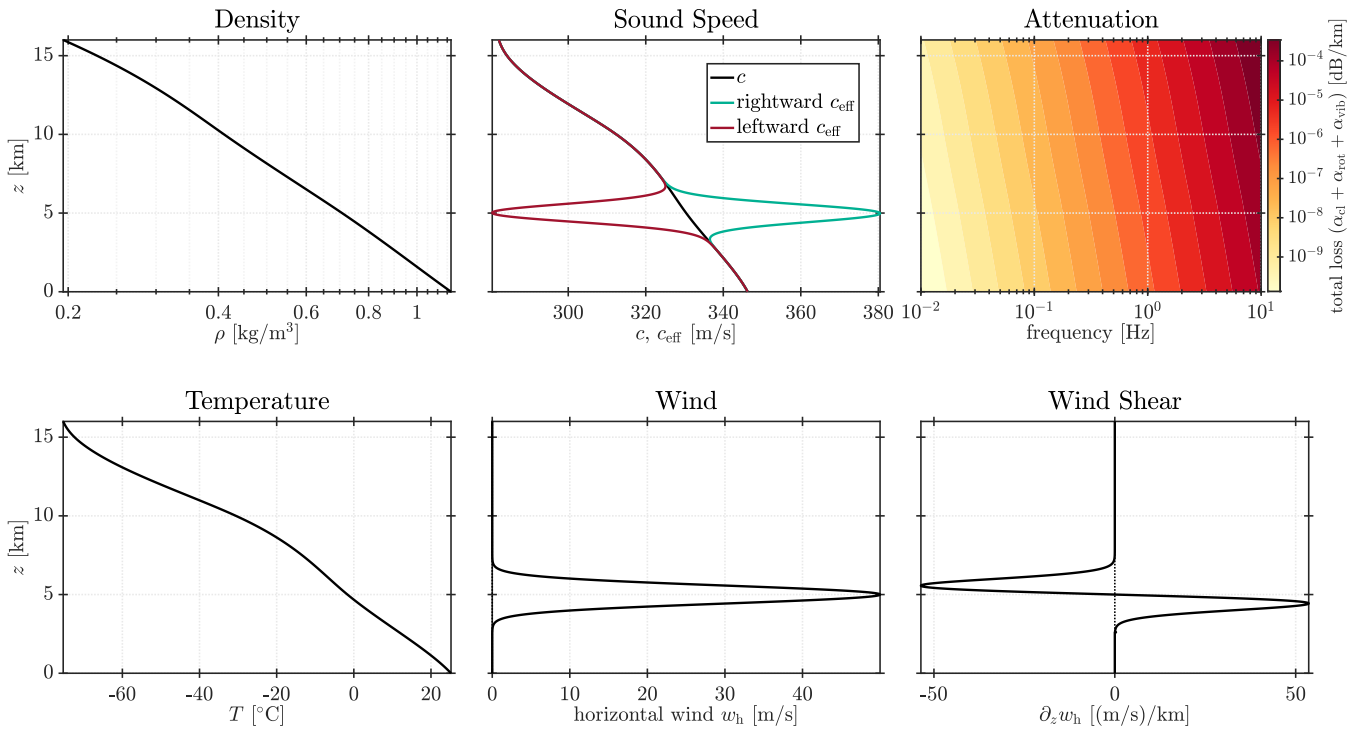


**Figure S5.** Realistic atmospheric model associated to the realistic topography case with wind jet. It is exactly the same model as the one presented in Figure S3 (see it for a description of the panels), apart from the wind. The wind here is chosen as a Gaussian jet of amplitude 50 m/s at altitude 5 km and with half-width 800 m:  $50 \exp\left(-\left(\frac{z-5000}{800}\right)^2\right)$ .

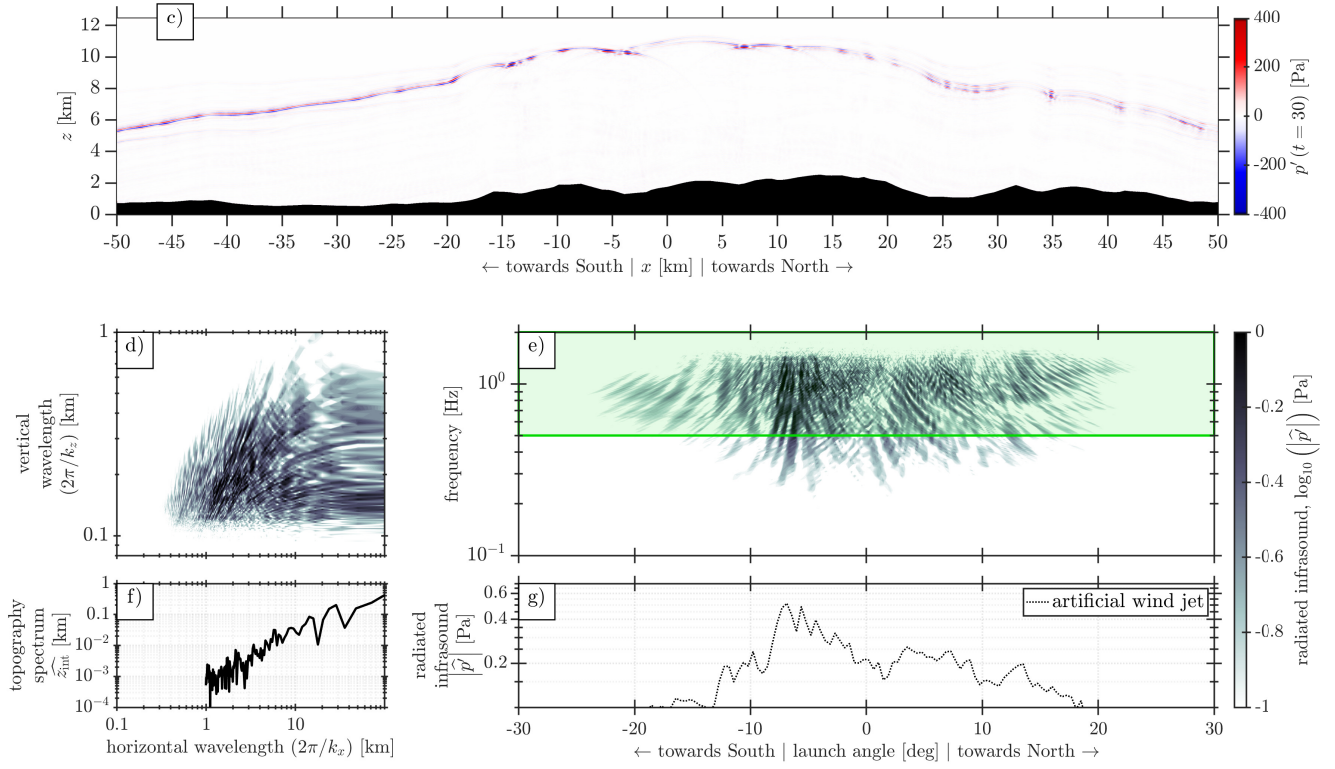


**Figure S6.** Summary of the scattering and radiation pattern study for the realistic topography case, with the atmosphere presented in Figure S5. See also Figure 7 in the main text for comparison. See caption of Figure S4 for a description of the panels.